Aeroelastic Prediction of Discrete Gust Loads Using Nonlinear and Time-Linearized CFD-Methods

(Received: Jan. 24, 2015. Revised: Oct. 12, 2015. Accepted: Dec. 16, 2015)

Mark Förster[1]
Christian Breitsamter[1]

Abstract

The small disturbance finite volume Navier-Stokes solver AER-SDNS is augmented by a discrete gust model. With AER-SDNS, complex Generalized Aerodynamic Forces (GAFs) are computed very efficiently in the frequency domain, while preserving the full Computational Fluid Dynamics (CFD) quality of the results. Finally, various aeroelastic gust responses are determined by solving a linear state space model. The results are compared to gust responses by means of an artificial velocity gust model and a strongly coupled, time domain, aeroelastic method. As test case, the low aspect ratio swept AGARD 445.6 wing is employed. Additionally, a flutter stability analysis is conducted in order to validate both methods.

1 Introduction

In aerospace engineering a gust is known to be a sudden change of induced air flow perpendicular to the flight path of the aircraft and hence a change in the resulting wind direction. In general, gusts can also act along the flight path creating loads especially on the flaps. The sudden and random induced angle of attack or sideslip can potentially cause structural damage or loss of control but in any case it causes fatigue and a reduction of passenger comfort. That is why gusts need to be considered during the aircraftdesign and verification process with respect to structural loads, stability and control. Furthermore, aeroelastic effects need to be included in the analysis process of flexible aircraft, since they also have a strong impact on the afore mentioned issues. As a relief, gust alleviation technology can lead to major aircraft performance improvements. Hence, it is of major interest to develop higly accurate and computationally efficient models for gust prediction.

Although aeroelastic methods have strongly progressed during the last decades [1], [2], [3], the standard tools used by industry are still based on potential flow methods due to their robustness and computational efficiency. Methods commonly used to predict gust loads are essentially based on the Küssner [4] and the Sears [5] function. One major drawback of potential flow methods is the insufficient prediction quality in the transonic flow regime. Wind tunnel testing including aeroelastic effects as well as specified gust excitation is rather challenging.

The application of Computational Fluid Dynamics (CFD) methods allows the accurate prediction of unsteady aerodynamic forces, especially in the transonic velocity range for complex aircraft configurations, where potential theory methods are known to be of less quality. As a result, uncertainties during the aeroelastic certification process can be reduced. Unfortunately, CFD-computations are rather expensive. One potential remedy is to apply appropriate Reduced Order Models (ROM) [6], [7].

In the present study, the small disturbance CFD-solver AER-SDNS [8], [9] is extended with a harmonic gust model derived from the formulation introduced in [10], in order to compute Generalized Aerodynamic Forces (GAFs) directly

[1] Institute of Aerodynamics and Fluid Mechanics, Technische Universität München
Boltzmannstrae 15, 85748 Garching bei München, Germany

doi:10.3293/asdj.2015.27

in the frequency domain. One important benefit is that the GAFs can be processed within the existing and well established aeroelastic and multidisciplinary design environments without any additional effort. Subsequently, the computed GAFs are used in a linear state space model to compute the time domain gust response. AER-SDNS combines the advantages of highly accurate CFD-results with computational efficiency. Furthermore, once an appropriate set of GAFs is computed, it can be used to compute gust responses to any kind of arbitrary gust excitation. The results are compared to the gust response computed by means of the in-house transient, non-linear solver AER-NS that is strongly coupled to the in-house structural solver AER-FE. For this purpose, AER-NS employs an artificial velocity gust model according to [11], [12]. As test case, the well known AGARD 445.6 wing is used [13]. First, a flutter stability computation is conducted to validate the linear and the nonlinear aeroelastic solver against experimental data. Finally, responses of the AGARD 445.6 wing are computed for several "1-cos"-gust excitations of varying length and amplitude.

2 Numerical Methods

In the following sections, the numerical characteristics of the small disturbance flow solver AER-SDNS, the nonlinear flow solver AER-NS, the structural solver AER-FE and the respective gust model is described in more detail. Subsequently, the methodology in time and frequency domain is presented, including the aeroelastic coupling procedure.

2.1 Nonlinear Flow Solver

The flow solver AER-NS [8], [9] is capable of performing unsteady, nonlinear and viscous CFD computations by solving the Navier-Stokes-equations. The Navier-Stokes-equations in conservation form are formulated as following

$$\frac{\partial \boldsymbol{q}}{\partial t} + \frac{\partial \boldsymbol{f}}{\partial x} + \frac{\partial \boldsymbol{g}}{\partial y} + \frac{\partial \boldsymbol{h}}{\partial z} = \frac{\partial \boldsymbol{f_v}}{\partial x} + \frac{\partial \boldsymbol{g_v}}{\partial y} + \frac{\partial \boldsymbol{h_v}}{\partial z}. \tag{1}$$

The state vector $\boldsymbol{q} = [\rho, \rho u, \rho v, \rho w, \rho e]^T$ is given in terms of the density ρ, the cartesian velocity components u, v, w, the specific total energy e and it is differentiated with respect to the time t. The convective fluxes $\boldsymbol{f}$, $\boldsymbol{g}$, $\boldsymbol{h}$ and the viscous fluxes $\boldsymbol{f_v}$, $\boldsymbol{g_v}$, $\boldsymbol{h_v}$ are formulated and differentiated with respect to the cartesian coordinates x, y, z. This system of partial differential equations can also be expressed in moving curvilinear coordinates $\xi = \xi(x, y, z, t)$, $\eta = \eta(x, y, z, t)$, $\zeta = \zeta(x, y, z, t)$, $\tau = t$,

$$\frac{\partial \boldsymbol{Q}}{\partial \tau} + \frac{\partial \boldsymbol{F}}{\partial \xi} + \frac{\partial \boldsymbol{G}}{\partial \eta} + \frac{\partial \boldsymbol{H}}{\partial \zeta} = \frac{\partial \boldsymbol{F_v}}{\partial \xi} + \frac{\partial \boldsymbol{G_v}}{\partial \eta} + \frac{\partial \boldsymbol{H_v}}{\partial \zeta}. \tag{2}$$

Then the fluxes are given in terms of the determinant of the coordinate transformation Jacobian J and the spatial and temporal metrics of the coordinate transformation ξ_t, ξ_x, ξ_y, ξ_z, η_t, η_x, η_y, η_z, ζ_t, ζ_x, ζ_y, ζ_z,

$$\begin{aligned} \boldsymbol{F} &= J\xi_t \boldsymbol{q} + J\xi_x \boldsymbol{f} + J\xi_y \boldsymbol{g} + J\xi_z \boldsymbol{h}, \\ \boldsymbol{G} &= J\eta_t \boldsymbol{q} + J\eta_x \boldsymbol{f} + J\eta_y \boldsymbol{g} + J\eta_z \boldsymbol{h}, \\ \boldsymbol{H} &= J\zeta_t \boldsymbol{q} + J\zeta_x \boldsymbol{f} + J\zeta_y \boldsymbol{g} + J\zeta_z \boldsymbol{h}, \end{aligned} \tag{3}$$

$$\begin{aligned} \boldsymbol{F_v} &= J\xi_x \boldsymbol{f_v} + J\xi_y \boldsymbol{g_v} + J\xi_z \boldsymbol{h_v}, \\ \boldsymbol{G_v} &= J\eta_x \boldsymbol{f_v} + J\eta_y \boldsymbol{g_v} + J\eta_z \boldsymbol{h_v}, \\ \boldsymbol{H_v} &= J\zeta_x \boldsymbol{f_v} + J\zeta_y \boldsymbol{g_v} + J\zeta_z \boldsymbol{h_v}. \end{aligned} \tag{4}$$

The new state vector is defined by $\boldsymbol{Q} = J\boldsymbol{q}$.

The numerical method employs a structured cell-centered finite volume descretization scheme. An upwind evaluation of the convective fluxes is realized with Roe's flux difference splitting scheme [14] and the viscous fluxes are evaluated according to Chakravarthy [15]. Second order spatial accuracy is realized with the monotonic-upstream-scheme-for-conservation-laws extrapolation while the total variation diminishing property is granted by means of the Van Albada limiter [16].

To perform time-accurate, fully nonlinear computations, a dual time stepping scheme with second order time accuracy is implemented [17], [9]

$$\begin{aligned}\left[\left(\frac{1}{\Delta\tau^*}+\frac{3}{2\Delta\tau}\right)J^{n+1}\bar{\bar{\boldsymbol{I}}}+\left.\frac{\partial \boldsymbol{R_k}}{\partial \boldsymbol{q}}\right|^n\right]\Delta\boldsymbol{q}=\\ -\left(\boldsymbol{R_k}^n+\boldsymbol{R_v}^n\right)-\frac{3\boldsymbol{Q}^{n+1,m}-4\boldsymbol{Q}^n+\boldsymbol{Q}^{n-1}}{2\Delta\tau},\end{aligned} \tag{5}$$

where τ^* is an artificial pseudo-time and the fluxes are replaced by

$$\boldsymbol{R_k}=\frac{\partial \boldsymbol{F}}{\partial\xi}+\frac{\partial \boldsymbol{G}}{\partial\eta}+\frac{\partial \boldsymbol{H}}{\partial\zeta}, \tag{6}$$

and

$$\boldsymbol{R_v}=-\frac{\partial \boldsymbol{F_v}}{\partial\xi}-\frac{\partial \boldsymbol{G_v}}{\partial\eta}-\frac{\partial \boldsymbol{H_v}}{\partial\zeta}, \tag{7}$$

respectively. The time integration is done implicitly by employing a lower-upper-symmetric-successive-overrelaxation algorithm [18].

The implemented boundary conditions are applicable for moving grids. The farfield boundary condition is realized by a characteristic boundary condition. In case of the no-slip condition, the contravariant velocities at the wall are set to zero [19]. The one equation Spalart-Allmaras turbulence model provides eddy viscosity closure [20].

2.2 Small Disturbance Flow Solver

The small disturbance Navier-Stokes solver AER-SDNS is based on the assumption that the unsteady flow responds harmonically to a harmonic body motion with change of amplitude and phase. Thus, this approach handles harmonic unsteady flow phenomena as linear perturbations about a non-linear steady state $\bar{\boldsymbol{q}}$ by means of a triple decomposition [8], [9]

$$\boldsymbol{q}(\tau,\xi,\eta,\zeta)=\bar{\boldsymbol{q}}(\xi,\eta,\zeta)+\tilde{\boldsymbol{q}}(\tau,\xi,\eta,\zeta)+\boldsymbol{q}'(\tau,\xi,\eta,\zeta). \tag{8}$$

An instantaneous flow state is separated into a steady state mean component $\bar{\boldsymbol{q}}(\xi,\eta,\zeta)$, a time dependent harmonic component $\tilde{\boldsymbol{q}}(\tau,\xi,\eta,\zeta)$ and a turbulent fluctuation $\boldsymbol{q}'(\tau,\xi,\eta,\zeta)$. The harmonic component is expressed in terms of the state vector amplitude $\hat{\boldsymbol{q}}$, the non-dimensional frequency k and the time τ

$$\tilde{\boldsymbol{q}}(\tau,\xi,\eta,\zeta)=\hat{\boldsymbol{q}}(\xi,\eta,\zeta)e^{ik\tau}. \tag{9}$$

The metrics are based on the spatial coordinates of the cell corner points which can also be separated into a reference and a perturbation part

$$\boldsymbol{x}(\tau,\xi,\eta,\zeta)=\bar{\boldsymbol{x}}(\xi,\eta,\zeta)+\tilde{\boldsymbol{x}}(\tau,\xi,\eta,\zeta). \tag{10}$$

Assuming harmonic motion of the body yields for the coordinates of the grid deformation

$$\tilde{\boldsymbol{x}}(\tau,\xi,\eta,\zeta)=\hat{\boldsymbol{x}}(\xi,\eta,\zeta)e^{ik\tau}, \tag{11}$$

and thus for the metric terms

$$\begin{aligned}\tilde{J}&=\hat{J}e^{ik\tau},\\ \widetilde{J\xi}_{t,x,y,z}&=\widehat{J\xi}_{t,x,y,z}e^{ik\tau},\\ \widetilde{J\eta}_{t,x,y,z}&=\widehat{J\eta}_{t,x,y,z}e^{ik\tau},\\ \widetilde{J\zeta}_{t,x,y,z}&=\widehat{J\zeta}_{t,x,y,z}e^{ik\tau}.\end{aligned} \tag{12}$$

The influence of higher order harmonics is neglected.

By substitution of the perturbation formulation (Eq. 10) for the grid deformation, the metrics and the field quantities into the full system of conservative Navier-Stokes-equations (Eq. 2), the following equation is obtained

$$\frac{\partial \hat{\boldsymbol{Q}}^{(1)}}{\partial \tau^*} + ik\hat{\boldsymbol{Q}}^{(1)} + \frac{\partial \hat{\boldsymbol{F}}^{(1)}}{\partial \xi} + \frac{\partial \hat{\boldsymbol{G}}^{(1)}}{\partial \eta} + \frac{\partial \hat{\boldsymbol{H}}^{(1)}}{\partial \zeta} - \frac{\partial \hat{\boldsymbol{F}}_{\boldsymbol{v}}{}^{(1)}}{\partial \xi} - \frac{\partial \hat{\boldsymbol{G}}_{\boldsymbol{v}}{}^{(1)}}{\partial \eta} - \frac{\partial \hat{\boldsymbol{H}}_{\boldsymbol{v}}{}^{(1)}}{\partial \zeta} = - ik\hat{\boldsymbol{Q}}^{(2)} - \frac{\partial \hat{\boldsymbol{F}}^{(2)}}{\partial \xi} - \frac{\partial \hat{\boldsymbol{G}}^{(2)}}{\partial \eta} - \frac{\partial \hat{\boldsymbol{H}}^{(2)}}{\partial \zeta} + \frac{\partial \hat{\boldsymbol{F}}_{\boldsymbol{v}}{}^{(2)}}{\partial \xi} + \frac{\partial \hat{\boldsymbol{G}}_{\boldsymbol{v}}{}^{(2)}}{\partial \eta} + \frac{\partial \hat{\boldsymbol{H}}_{\boldsymbol{v}}{}^{(2)}}{\partial \zeta}, \tag{13}$$

with

$$\begin{aligned}
\hat{\boldsymbol{Q}}^{(1)} &= \bar{J}\hat{\boldsymbol{q}}, \\
\hat{\boldsymbol{Q}}^{(2)} &= \hat{J}\bar{\boldsymbol{q}}, \\
\hat{\boldsymbol{F}}^{(1)} &= \overline{J\xi_t}\hat{\boldsymbol{q}} + \overline{J\xi_x}\hat{\boldsymbol{f}} + \overline{J\xi_y}\hat{\boldsymbol{g}} + \overline{J\xi_z}\hat{\boldsymbol{h}}, \\
\hat{\boldsymbol{F}}^{(2)} &= \widehat{J\xi_t}\bar{\boldsymbol{q}} + \widehat{J\xi_x}\bar{\boldsymbol{f}} + \widehat{J\xi_y}\bar{\boldsymbol{g}} + \widehat{J\xi_z}\bar{\boldsymbol{h}}, \\
\hat{\boldsymbol{G}}^{(1)} &= \overline{J\eta_t}\hat{\boldsymbol{q}} + \overline{J\eta_x}\hat{\boldsymbol{f}} + \overline{J\eta_y}\hat{\boldsymbol{g}} + \overline{J\eta_z}\hat{\boldsymbol{h}}, \\
\hat{\boldsymbol{G}}^{(2)} &= \widehat{J\eta_t}\bar{\boldsymbol{q}} + \widehat{J\eta_x}\bar{\boldsymbol{f}} + \widehat{J\eta_y}\bar{\boldsymbol{g}} + \widehat{J\eta_z}\bar{\boldsymbol{h}}, \\
\hat{\boldsymbol{H}}^{(1)} &= \overline{J\zeta_t}\hat{\boldsymbol{q}} + \overline{J\zeta_x}\hat{\boldsymbol{f}} + \overline{J\zeta_y}\hat{\boldsymbol{g}} + \overline{J\zeta_z}\hat{\boldsymbol{h}}, \\
\hat{\boldsymbol{H}}^{(2)} &= \widehat{J\zeta_t}\bar{\boldsymbol{q}} + \widehat{J\zeta_x}\bar{\boldsymbol{f}} + \widehat{J\zeta_y}\bar{\boldsymbol{g}} + \widehat{J\zeta_z}\bar{\boldsymbol{h}}, \\
\hat{\boldsymbol{F}}_{\boldsymbol{v}}{}^{(1)} &= \overline{J\xi_x}\hat{\boldsymbol{f}}_{\boldsymbol{v}} + \overline{J\xi_y}\hat{\boldsymbol{g}}_{\boldsymbol{v}} + \overline{J\xi_z}\hat{\boldsymbol{h}}_{\boldsymbol{v}}, \\
\hat{\boldsymbol{F}}_{\boldsymbol{v}}{}^{(2)} &= \widehat{J\xi_x}\bar{\boldsymbol{f}}_{\boldsymbol{v}} + \widehat{J\xi_y}\bar{\boldsymbol{g}}_{\boldsymbol{v}} + \widehat{J\xi_z}\bar{\boldsymbol{h}}_{\boldsymbol{v}}, \\
\hat{\boldsymbol{G}}_{\boldsymbol{v}}{}^{(1)} &= \overline{J\eta_x}\hat{\boldsymbol{f}}_{\boldsymbol{v}} + \overline{J\eta_y}\hat{\boldsymbol{g}}_{\boldsymbol{v}} + \overline{J\eta_z}\hat{\boldsymbol{h}}_{\boldsymbol{v}}, \\
\hat{\boldsymbol{G}}_{\boldsymbol{v}}{}^{(2)} &= \widehat{J\eta_x}\bar{\boldsymbol{f}}_{\boldsymbol{v}} + \widehat{J\eta_y}\bar{\boldsymbol{g}}_{\boldsymbol{v}} + \widehat{J\eta_z}\bar{\boldsymbol{h}}_{\boldsymbol{v}}, \\
\hat{\boldsymbol{H}}_{\boldsymbol{v}}{}^{(1)} &= \overline{J\zeta_x}\hat{\boldsymbol{f}}_{\boldsymbol{v}} + \overline{J\zeta_y}\hat{\boldsymbol{g}}_{\boldsymbol{v}} + \overline{J\zeta_z}\hat{\boldsymbol{h}}_{\boldsymbol{v}}, \\
\hat{\boldsymbol{H}}_{\boldsymbol{v}}{}^{(2)} &= \widehat{J\zeta_x}\bar{\boldsymbol{f}}_{\boldsymbol{v}} + \widehat{J\zeta_y}\bar{\boldsymbol{g}}_{\boldsymbol{v}} + \widehat{J\zeta_z}\bar{\boldsymbol{h}}_{\boldsymbol{v}}.
\end{aligned} \tag{14}$$

The terms indicated by superscript (1) denote products of the metrics referring to the reference grid and the perturbed flow quantities while (2) corresponds to products of the disturbed metrics multiplied by the steady state flow quantities. Hence the terms indicated by (2) are initially known and represent a right hand side source term of Eq. 13.

AER-SDNS computes the amplitude and phase shift of the unsteady flow quantities directly in the frequency domain with full CFD quality of the results. Two grids need to be provided, one grid prescribing the undisturbed reference position of the body and the other grid defining the deflected extremum position or a deformed elastic shape of the body. Furthermore, a steady state solution serving as the time-invariant mean flow field must be provided.

The main advantage of the small disturbance solver is the treatment of an unsteady problem by a quasi-steady formulation. Hence, a considerable reduction of computational time by an order of magnitude is accomplished compared to the respective time marching computation. The spatial discretization, the placement of appropriate boundary conditions [21] and the turbulence modeling formally corresponds to the methods mentioned for the nonlinear solver under the premise of appropriate linearization. A more elaborate demonstration of the entire linearization process including the turbulence modeling is presented in [8], [9].

The time integration of the discretized system of equations is accomplished

by means of an artificial pseudo-time τ^*

$$\left[\bar{J}(\Delta\tau^{*-1} + ik)\bar{\bar{I}} + \left.\frac{\partial \boldsymbol{R}}{\partial \boldsymbol{q}}\right|_{\bar{q}}\right] \Delta\hat{\boldsymbol{q}} = -\hat{\boldsymbol{R}}^{(1)n} - \hat{\boldsymbol{R}}^{(2)}, \tag{15}$$

with

$$\hat{\boldsymbol{R}}^{(1)} = ik\hat{\boldsymbol{Q}}^{(1)} + \frac{\partial \hat{\boldsymbol{F}}^{(1)}}{\partial \xi} + \frac{\partial \hat{\boldsymbol{G}}^{(1)}}{\partial \eta} + \frac{\partial \hat{\boldsymbol{H}}^{(1)}}{\partial \zeta} - \frac{\partial \hat{\boldsymbol{F}}_{\boldsymbol{v}}{}^{(1)}}{\partial \xi} - \frac{\partial \hat{\boldsymbol{G}}_{\boldsymbol{v}}{}^{(1)}}{\partial \eta} - \frac{\partial \hat{\boldsymbol{H}}_{\boldsymbol{v}}{}^{(1)}}{\partial \zeta}, \tag{16}$$

and

$$\hat{\boldsymbol{R}}^{(2)} = ik\hat{\boldsymbol{Q}}^{(2)} + \frac{\partial \hat{\boldsymbol{F}}^{(2)}}{\partial \xi} + \frac{\partial \hat{\boldsymbol{G}}^{(2)}}{\partial \eta} + \frac{\partial \hat{\boldsymbol{H}}^{(2)}}{\partial \zeta} - \frac{\partial \hat{\boldsymbol{F}}_{\boldsymbol{v}}{}^{(2)}}{\partial \xi} - \frac{\partial \hat{\boldsymbol{G}}_{\boldsymbol{v}}{}^{(2)}}{\partial \eta} - \frac{\partial \hat{\boldsymbol{H}}_{\boldsymbol{v}}{}^{(2)}}{\partial \zeta}. \tag{17}$$

2.3 Gust Modeling

Several approaches for gust modelling in time-accurate CFD-simulations can be found in the literature [11], [12], [23]. The most straight-forward approach would be to impose the gust velocity profile at the inflow boundary of the computational domain. The main advantage is that interactions between the gust and the flow solution become possible. But this method is also accompanied by significant numerical problems. The grid resolution has to be very fine throughout great parts of the farfield region since the gust profile has to convect from the upstream boundary through the computational domain to the nearfield. On the one hand, this increases the simulation time and, on the other hand, it is hard to preserve a specific gust velocity profile and amplitude due to numerical dissipation. An artificial velocity approach has been shown to be more admissible [11], [12]. This method is based on an artificial local gust velocity u_G, v_G, w_G added to the cell midpoint velocities x_τ, y_τ, z_τ within the entire domain. Hence, the gust velocities directly affect the metrics

$$\begin{aligned} J\xi_t &= -J\xi_x(x_\tau + u_G) - J\xi_y(y_\tau + v_G) - J\xi_z(z_\tau + w_G), \\ J\eta_t &= -J\eta_x(x_\tau + u_G) - J\eta_y(y_\tau + v_G) - J\eta_z(z_\tau + w_G), \\ J\zeta_t &= -J\zeta_x(x_\tau + u_G) - J\zeta_y(y_\tau + v_G) - J\zeta_z(z_\tau + w_G). \end{aligned} \tag{18}$$

This manipulation corresponds to a rigid body motion that is imposed locally at every grid point, although the grid remains steady. Hence, the gust shape and translational motion can be imposed directly at the body where the grid resolution is very fine.

Analogously, this artificial velocity approach can be applied to the small disturbance solver AER-SDNS. The fundamental requirement for this approach is again a linear, harmonic perturbation about the nonlinear, time-invariant mean flow field. A complex expression for a sinusoidal gust velocity profile traveling in x-direction is given by

$$\widetilde{\boldsymbol{v}_G}(t, x) = \boldsymbol{v}_G e^{i\omega\left(t - \frac{\boldsymbol{x} - \boldsymbol{x_{ref}}}{U_\infty}\right)}. \tag{19}$$

If the time dependency is eliminated, the following gust velocity profile $\widehat{\boldsymbol{v}_G}$ is obtained in terms of the reduced frequency $k_{red} = \omega l_{ref}/U_\infty$ with l_{ref} being the reference length and U_∞ being the free stream velocity

$$\widehat{\boldsymbol{v}_G}(x, y, z) = \boldsymbol{v}_G(x, y, z) e^{ik_{red}\left(\frac{\boldsymbol{x} - \boldsymbol{x_{ref}}}{l_{ref}}\right)}. \tag{20}$$

Then the components $\widehat{u_G}$, $\widehat{v_G}$, $\widehat{w_G}$ of the gust induced velocity vector $\widehat{\boldsymbol{v}_G}$ are added to the grid velocities $\widehat{x_\tau}$, $\widehat{y_\tau}$, $\widehat{z_\tau}$ of the perturbed state. The cell face velocities $\widehat{J\xi_t}$, $\widehat{J\eta_t}$, $\widehat{J\zeta_t}$ of the linearized metrics are defined as

$$\begin{aligned} \widehat{J\xi_t} &= -\overline{J\xi_x}(\widehat{x_\tau} + \widehat{u_G}) - \overline{J\xi_y}(\widehat{y_\tau} + \widehat{v_G}) - \overline{J\xi_z}(\widehat{z_\tau} + \widehat{w_G}), \\ \widehat{J\eta_t} &= -\overline{J\eta_x}(\widehat{x_\tau} + \widehat{u_G}) - \overline{J\eta_y}(\widehat{y_\tau} + \widehat{v_G}) - \overline{J\eta_z}(\widehat{z_\tau} + \widehat{w_G}), \\ \widehat{J\zeta_t} &= -\overline{J\zeta_x}(\widehat{x_\tau} + \widehat{u_G}) - \overline{J\zeta_y}(\widehat{y_\tau} + \widehat{v_G}) - \overline{J\zeta_z}(\widehat{z_\tau} + \widehat{w_G}), \end{aligned} \tag{21}$$

and the amplitudes of the grid point velocities are given by

$$\begin{aligned} \widehat{x_\tau} &= ik\hat{x}, \\ \widehat{y_\tau} &= ik\hat{y}, \\ \widehat{z_\tau} &= ik\hat{z}. \end{aligned} \tag{22}$$

Because $\boldsymbol{v}_G$ is a complex quantity, the cell face velocities have both a real and an imaginary part now. It is inherently accounted for in the convective flux vector evaluation and in the no-slip boundary condition.

2.4 Structural Solver

The structural solver AER-FE is based on a geometrically linear FEM (Finite Element Method) and is capable of a static, modal, frequency-response and transient analysis for several element types. The fundamental semi-discrete system of equations obtained from the FEM and describing the motion of an elastic body is given by

$$\bar{\bar{\boldsymbol{M}}}\ddot{\boldsymbol{d}}(t) + \bar{\bar{\boldsymbol{C}}}\dot{\boldsymbol{d}}(t) + \bar{\bar{\boldsymbol{K}}}\boldsymbol{d}(t) = \boldsymbol{F}(t), \tag{23}$$

wherein $\boldsymbol{d}(t)$, $\boldsymbol{F}(t)$, $\bar{\bar{\boldsymbol{M}}}$, $\bar{\bar{\boldsymbol{C}}}$ and $\bar{\bar{\boldsymbol{K}}}$ are respectively the displacement vector, the external force vector, the mass matrix, the damping matrix and the stiffness matrix. The transient analysis is formulated in modal space to decouple the system of ordinary equations and reduce computational effort. It is assumed that the motion of the structure is dominated by a small number of low frequency eigenmodes, while high frequency modes can be neglected. After the transformation $\boldsymbol{d} = \bar{\bar{\boldsymbol{\Phi}}}\boldsymbol{q}$ into modal space , Eq. 23 becomes

$$\ddot{q}_i(t) + 2\zeta_i\omega_i\dot{q}_i(t) + \omega_i^2 q_i(t) = F_i(t). \tag{24}$$

Subscript i designates each modal degree of freedom, with q being the modal displacement, ω_i being the modal eigenfrequency, ζ_i being the modal damping ratio and $\bar{\bar{\boldsymbol{\Phi}}}$ is the eigenvector matrix. This system of equations can be converted to state space form as

$$\begin{pmatrix} \dot{q}_i \\ \ddot{q}_i \end{pmatrix} = \begin{bmatrix} 0 & 1 \\ -\omega_i^2 & -2\zeta_i\omega_i \end{bmatrix} \begin{pmatrix} q_i \\ \dot{q}_i \end{pmatrix} + \begin{pmatrix} 0 \\ F_i \end{pmatrix}, \tag{25}$$

or compactly as

$$\frac{\partial \boldsymbol{q}}{\partial t} = \boldsymbol{R}. \tag{26}$$

The time integration is achieved using a second order dual time stepping procedure [22] in accordance to the flow solver

$$\left[\left(\frac{1}{\Delta\tau^*} + \frac{3}{2\Delta t}\right)\bar{\bar{\boldsymbol{I}}} + \left.\frac{\partial \boldsymbol{R}}{\partial \boldsymbol{q}}\right|^n\right]\Delta\boldsymbol{q} = \boldsymbol{R}^{n+1,m} - \frac{3\boldsymbol{q}^{n+1,m} - 4\boldsymbol{q}^n + \boldsymbol{q}^{n-1}}{2\Delta t}. \tag{27}$$

2.5 Aeroelastic Coupling in the Time Domain

For the present investigations, the flow solver AER-NS and the structural solver AER-FE are coupled to perform time-accurate aeroelastic simulations. Since both solvers are based on different numerical discretization techniques, care must be taken with respect to the transfer of loads and changes in geometry between both solvers in order to preserve the sum of energy in the overall system. In such a partitioned approach, the structural grid and the flow surface grid usually differ in their discretization and shape. Hence, an appropriate time sequencing between both solvers as well as an appropriate interpolation of aerodynamic loads and structural deformations is required to guarantee a conservative numerical scheme.

The load transfer is realized by using finite element shape functions to transform the surface loads created by the finite volume flow solver into consistent structural nodal forces [24]. The surface deformation transfer from the structural grid to the fluid grid is accomplished by the thin-plate-spline method [25]. Another challenging task that comes along with the deformation of the body surface is the deformation of the volume grid. In order to realize this most efficiently, the spring-analogy method is used to deform the multiblock corner points and transfinite interpolation is applied to the interior vertices of the blocks according to [26].

The aeroelastic coupling between the structural and the flow solver with respect to the time integration is imposed by means of a strong coupling. One advantage of the dual-time-stepping formulation implemented for both solvers is that information can be exchanged arbitrarily in pseudo-time without affecting the time accuracy of the aeroelastic solution [22].

2.6 Aeroelastic Coupling in the Frequency Domain

Every dynamic system that is characterized by a feedback loop is capable of executing oscillations about a mean value. Since any kind of periodic signal can be represented by a number of distinct harmonic signals, a transformation into the frequency domain is often beneficial to simplify the mathematical treatment. Regarding Eq. 23, the forces $\boldsymbol{F}(t)$ can be separated into aerodynamic feedback forces $\boldsymbol{F}_A$ and external forces like gust loads $\boldsymbol{F}_G$. As long as the aerodynamic forces depend linearly on the structural deformations $\boldsymbol{d}(t)$, which is also assumed in the mathematical formulation of the linearized CFD-solver, the system of equations can be written as

$$\bar{\bar{\boldsymbol{M}}}\ddot{\boldsymbol{d}}(t) + \bar{\bar{\boldsymbol{C}}}\dot{\boldsymbol{d}}(t) + \bar{\bar{\boldsymbol{K}}}\boldsymbol{d}(t) - \boldsymbol{F}_A(\boldsymbol{d}(t)) = \boldsymbol{F}_G(t). \tag{28}$$

Subsequently, Eq. 28 is transformed into modal space and into Laplacian-space

$$\left[s^2\bar{\bar{\mathbb{M}}} + s\bar{\bar{\mathbb{C}}} + \bar{\bar{\mathbb{K}}} - q_\infty\bar{\bar{\mathbb{Q}}}_{ee}(s)\right]\boldsymbol{q}(s) = \frac{q_\infty}{U_\infty}\mathbb{Q}_{eG}(s)v_G(s). \tag{29}$$

Now the algebraic system of equations depends on the Laplace-variable s and is solely coupled by the displacement induced GAFs $\bar{\bar{\mathbb{Q}}}_{ee}(s)$. The term $\mathbb{Q}_{eG}(s)$ corresponds to the GAFs originating from the harmonic gust excitation and q_∞ is the dynamic pressure.

The GAF-matrices can be interpreted as forces that perform work in the direction of the structural degrees of freedom. In the present study, they are computed using AER-SDNS. As a result, the quality of the prediction in the transonic regime is better than the results provided by potential methods and the approach is more efficient than an unsteady coupled simulation in the time domain. AER-SDNS computes the real part $\Re(\hat{c}_p)$ and the imaginary part $\Im(\hat{c}_p)$ of the complex amplitude of the unsteady pressure distribution corresponding to the in-phase or the quasi-steady part of the response and the out-of-phase or the unsteady part of the response. For each eigenmode i and for each reduced frequency k_{red}, a single small disturbance CFD-run must be executed. Subsequently, the resulting pressure distribution c_p is projected onto the eigenmodes j given in terms of the displacement vector $\Delta\boldsymbol{d}_j$ and integrated over the body surface $\boldsymbol{S}_i$, leading to square GAF-matrices of dimensions i and j

$$\bar{\bar{\mathbb{Q}}}_{ee,ij}(ik_{red}) = \int_S \bar{c}_{p,i}\Delta\hat{\boldsymbol{d}}_j^T\, d\hat{\boldsymbol{S}}_i + \int_S \Re(\hat{c}_{p,i})\Delta\hat{\boldsymbol{d}}_j^T\, d\bar{\boldsymbol{S}}_i + \int_S \Im(\hat{c}_{p,i})\Delta\hat{\boldsymbol{d}}_j^T\, d\bar{\boldsymbol{S}}_i. \tag{30}$$

The shear stresses due to viscous effects are neglected. The GAFs corresponding to the gust excitation are normalized by the gust velocity and form the vector

$$\mathbb{Q}_{eG,j}(ik_{red}) = \frac{1}{\hat{v}_G}\int_S \Re(\hat{c}_p)\Delta\hat{\boldsymbol{d}}_j^T\, d\bar{\boldsymbol{S}} + \frac{1}{\hat{v}_G}\int_S \Im(\hat{c}_p)\Delta\hat{\boldsymbol{d}}_j^T\, d\bar{\boldsymbol{S}}. \tag{31}$$

The harmonic GAFs $\bar{\bar{\mathbb{Q}}}(ik_{red})$ result from the reduction of the transient motion in the Laplace domain to harmonic motion in the k-domain. The reduced frequency is related to the Laplace variable by $ik_{red} = sl/U_\infty$.

In order to compute the time domain response of the modeled aeroelastic system, Eq. 29 needs to be transformed back into time domain. Due to the fact that the GAFs are only available at discrete reduced frequencies, they need to be interpolated appropriately. Therefore, the RFA-method (Rational Function Approximation) of Roger [27] is applied, where the complex GAF-matrices are approximated by rational functions in the Laplace domain based on the coefficient matrices $\bar{\bar{\boldsymbol{A}}}_{ee}$

$$\bar{\bar{\mathbb{Q}}}_{ee}(p)\boldsymbol{q}(s) \approx \left[\bar{\bar{\boldsymbol{A}}}_{ee0} + \bar{\bar{\boldsymbol{A}}}_{ee1}p + \bar{\bar{\boldsymbol{A}}}_{ee2}p^2 + \sum_{j=3}^{N} \frac{\bar{\bar{\boldsymbol{A}}}_{eej}p}{p+\gamma_{j-2}}\right]\boldsymbol{q}(s), \tag{32}$$

with $p = sl/U_\infty$ being the non-dimensional Laplace-variable and γ_{j-2} representing the poles. One disadvantage of the RAF is the introduction of additional aerodynamic lag-states $\boldsymbol{q}_{ej}(s)$ that enhance the rank of the resulting state space model

$$\boldsymbol{q}_{ej}(s) = \frac{s}{s+\frac{U_\infty}{l}\gamma_{j-2}}\boldsymbol{q}(s). \tag{33}$$

The number of lag-states can be chosen arbitrarily by the user. In the present study, it is set to four additional states. The gust induced GAFs are approximated by

$$\mathbb{Q}_{eG}(p)v_G(s) \approx \left[\boldsymbol{A}_{eG0} + \boldsymbol{A}_{eG1}p + \sum_{j=3}^{N} \frac{\boldsymbol{A}_{eGj}p}{p+\gamma_{j-2}}\right]v_G(s), \tag{34}$$

with

$$q_{Gj}(s) = \frac{s}{s+\frac{U_\infty}{l}\gamma_{j-2}}v_G(s). \tag{35}$$

The system depencence on the second time derivate of the gust induced velocity is neglected. Substitution of Eq. 32 - Eq. 35 into Eq. 28 yields

$$\begin{aligned}\left[s^2\bar{\bar{\mathbb{M}}} + s\bar{\bar{\mathbb{C}}} + \bar{\bar{\mathbb{K}}}\right]\boldsymbol{q}(s) = q_\infty &\left[\left(\bar{\bar{\boldsymbol{A}}}_{ee0} + \bar{\bar{\boldsymbol{A}}}_{ee1}p + \bar{\bar{\boldsymbol{A}}}_{ee2}p^2\right)\boldsymbol{q}(s) + \sum_{j=3}^{N}\bar{\bar{\boldsymbol{A}}}_{eej}\boldsymbol{q}_{ej}(p)\right] \\ &+ \frac{q_\infty}{U_\infty}\left[\left(\boldsymbol{A}_{eG0} + \boldsymbol{A}_{eG1}p\right)v_G(s) + \sum_{j=3}^{N}\boldsymbol{A}_{eGj}q_{Gj}(p)\right].\end{aligned} \tag{36}$$

Finally, this system of equations is transformed into a linear, time-invariant

state space model [28]

$$\begin{Bmatrix} \dot{\boldsymbol{q}} \\ \ddot{\boldsymbol{q}} \\ \dot{\boldsymbol{q}}_{e3} \\ \vdots \\ \dot{\boldsymbol{q}}_{e7} \\ \dot{q}_{G3} \\ \vdots \\ \dot{q}_{G7} \end{Bmatrix} = \begin{bmatrix} 0 & 0 \\ \frac{q_\infty}{U_\infty} \bar{\bar{\boldsymbol{M}}}' \boldsymbol{A}_{eG0} & \frac{q_\infty l}{U_\infty^2} \bar{\bar{\boldsymbol{M}}}' \boldsymbol{A}_{eG1} \\ 0 & 0 \\ \vdots & \vdots \\ 0 & 0 \\ 0 & 1 \\ \vdots & \vdots \\ 0 & 1 \end{bmatrix} \begin{Bmatrix} v_G \\ \dot{v}_G \end{Bmatrix} + \begin{bmatrix} 0 & \bar{\bar{\boldsymbol{I}}} \\ \bar{\bar{\boldsymbol{M}}}' \bar{\bar{\boldsymbol{K}}}' & \bar{\bar{\boldsymbol{M}}}' \bar{\bar{\boldsymbol{C}}}' \\ 0 & \bar{\bar{\boldsymbol{I}}} \\ \vdots & \vdots \\ 0 & \bar{\bar{\boldsymbol{I}}} \\ 0 & 0 \\ \vdots & \vdots \\ 0 & 0 \end{bmatrix} \tag{37}$$

$$\begin{bmatrix} 0 & \cdots & 0 & 0 & \cdots & 0 \\ q_\infty \bar{\bar{\boldsymbol{M}}}' \bar{\bar{\boldsymbol{A}}}_{ee3} & \cdots & q_\infty \bar{\bar{\boldsymbol{M}}}' \bar{\bar{\boldsymbol{A}}}_{ee7} & \frac{q_\infty}{U_\infty} \bar{\bar{\boldsymbol{M}}}' \boldsymbol{A}_{eG3} & \cdots & \frac{q_\infty}{U_\infty} \bar{\bar{\boldsymbol{M}}}' \boldsymbol{A}_{eG7} \\ -\frac{U_\infty}{l} \gamma_1 \bar{\bar{\boldsymbol{I}}} & & 0 & 0 & \cdots & 0 \\ & \ddots & & \vdots & \ddots & \vdots \\ 0 & & -\frac{U_\infty}{l} \gamma_4 \bar{\bar{\boldsymbol{I}}} & 0 & \cdots & 0 \\ 0 & \cdots & 0 & -\frac{U_\infty}{l} \gamma_1 & & 0 \\ \vdots & \ddots & \vdots & & \ddots & \\ 0 & \cdots & 0 & 0 & & -\frac{U_\infty}{l} \gamma_4 \end{bmatrix} \begin{Bmatrix} \boldsymbol{q} \\ \dot{\boldsymbol{q}} \\ \boldsymbol{q}_{e3} \\ \vdots \\ \boldsymbol{q}_{e7} \\ q_{G3} \\ \vdots \\ q_{G7} \end{Bmatrix},$$

with

$$\begin{aligned} \bar{\bar{\boldsymbol{M}}}' &= \left[\bar{\mathbb{M}} - \frac{q_\infty l^2}{U_\infty^2} \bar{\bar{\boldsymbol{A}}}_{ee2} \right]^{-1}, \\ \bar{\bar{\boldsymbol{C}}}' &= \frac{q_\infty l}{U_\infty} \bar{\bar{\boldsymbol{A}}}_{ee1} - \bar{\mathbb{C}}, \\ \bar{\bar{\boldsymbol{K}}}' &= q_\infty \bar{\bar{\boldsymbol{A}}}_{ee0} - \bar{\mathbb{K}}. \end{aligned} \tag{38}$$

By means of the resulting state space model, it is possible to compute the coupled aeroelastic system response for any arbitrary gust excitation very efficiently, provided that the respective GAFs are already available.

3 Results

The results chapter is devided into three parts. First, the test case and the corresponding numerical model is described. Then a stability analysis is conducted in order to validate the aeroelastic methods against experimental data. Finally, aeroelastic responses to several gust inputs are presented and analyzed.

3.1 Test Case Description: Low-Aspect-Ratio Swept Wing - AGARD 445.6

The AGARD 445.6 wing, a well known test case within the aeroelastic community, is used to validate the presented methods. During the 1960's, flutter investigations were conducted at the Transonic Dynamics Tunnel at the NASA Langley Research Center in Hampton, Virginia [13]. Within the scope of this study, subsonic, transonic and supersonic experiments were conducted in air and Freon-12 for several wing configurations. The AGARD 445.6 test case is a low-aspect-ratio swept wing with a NACA 65A004 airfoil, see Tab. 1 and Fig. 1. In the present work the "weakened model 3"-test case is chosen utilizing air as the flow medium. The associated material properties conform to the experimentally determined data according to [13], as well as on numerically optimized data according to [29], see Tab. 2.

The structural model of the AGARD 445.6 wing is formulated in modal space. Therefore, a FEM-model is generated with AER-FE and a modal analysis

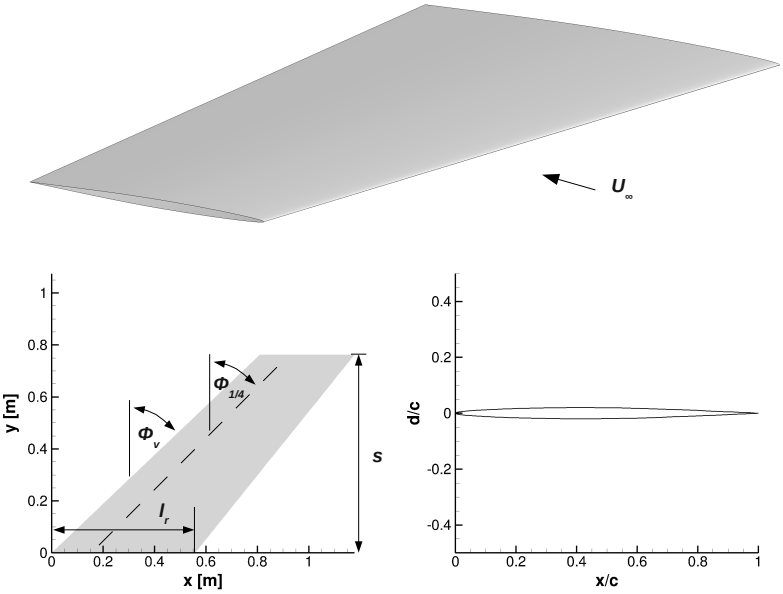

Figure 1: AGARD 445.6 wing in top view, side view and parametric view

Table 1: Geometric properties of the AGARD 445.6 wing

Semi span s	$762\,mm$
Root chord length l_r	$558.7\,mm$
Aerodynamic mean chord length l_μ	$470.4\,mm$
Aspect ratio Λ	1.65
Taper ratio λ	0.66
Leading edge sweep angle ϕ_v	46.3°
Quarter chord sweep angle $\phi_{1/4}$	45°
Maximum airfoil thickness d/c	4 %

Table 2: Material properties of the AGARD 445.6 wing

Young's modulus in spanwise direction E_{11}	$3.1511\,GPa$
Young's modulus in chordwise direction E_{22}	$0.4162\,GPa$
Young's modulus in thickness direction E_{33}	$0.4162\,GPa$
Angle of the fiber against free stream ϕ	45°
Shear modulus G	$0.4392\,GPa$
Poisson's ratio ν	0.31
Material density ρ	$381.98\,kg/m^3$

Mode	Mode shape	Eigenfrequency in $[Hz]$ Experiment [13]	computed (AER-FE)
1	1. Bending	9.60	9.64
2	1. Torsion	38.17	37.88
3	2. Bending	48.35	48.84
4	2. Torsion	91.54	97.74
5	3. Bending	118.11	123.49

Table 3: Eigenfrequencies of the AGARD 445.6 wing

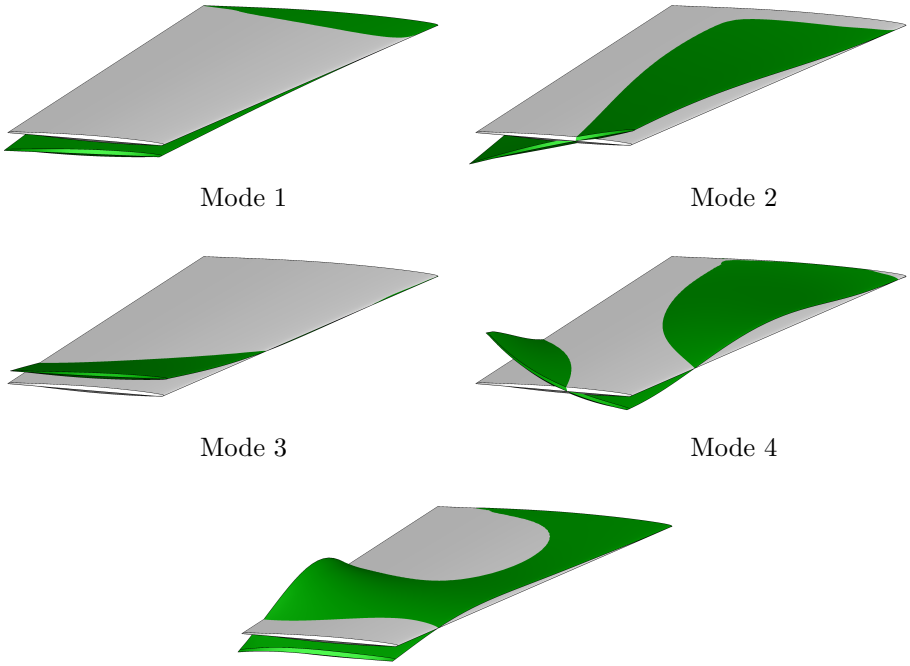

Figure 2: Eigenmodes of the AGARD 445.6 wing

is conducted. The planform of the wing is discretized by 600 quadrilateral Kirchhoff plate elements of varying thickness. The total wing mass is $m = 1.86\ kg$ according to the original wind tunnel model [13]. The modal model comprises the five lowest modes, namely three bending modes und two torsion modes. The eigenfrequencies are listed in Tab. 3 and the corresponding eigenforms are shown in Fig. 2, indicated by the green color in contrast to the undeformed wing shape in grey color. A comparison of the modal properties provided by the numerical model shows good agreement with the experimental data according to [13].

Additionally, a structured CFD-grid is generated. The grid consists of two blocks forming a C-H-topology as shown in Fig. 3. The surface grid is discretized by 144×48 cells and the computational domain is discretized by a total of 559000 volume grid points. A mesh convergence study has been conducted in [30]. A symmetry boundary condition is set on the semi-span plane next to the wing root. The farfield boundary has a distance of at least 10 semi-spans to the wing surface.

3.2 Stability Analysis in the Time and the Frequency Domain

The primary intention of this section is to validate the numerical model which is generated with the focus on capturing the general physics and dynamics of the "weakened model 3" AGARD 445.6 dynamic aeroelastic test case. For this test case, critical flutter data is provided at free stream conditions, see Tab.

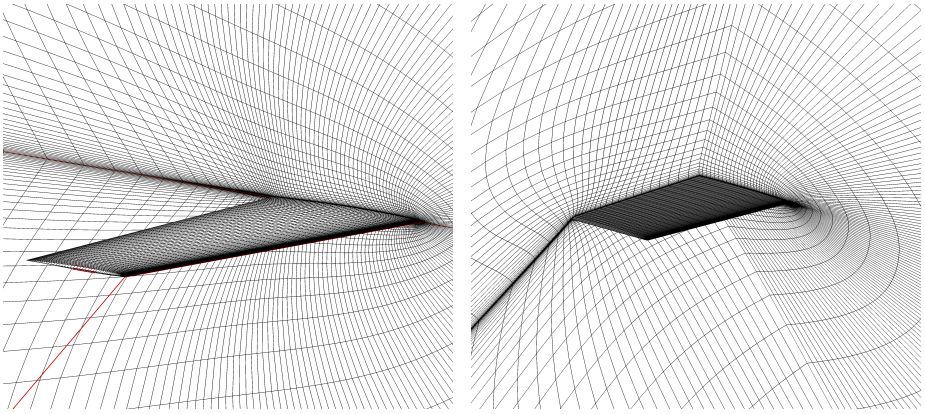

Figure 3: CFD-grid of the AGARD 445.6 wing

Table 4: Free stream conditions for the investigated AGARD 445.6 test case

Mach number M_∞	Density ρ_∞ in kg/m^3	Reynolds number Re
0.499	0.4278	2244905
0.678	0.2082	1494972
0.901	0.0995	968456
0.960	0.0634	661977
1.072	0.0551	641039
1.141	0.0783	983704

4 [13]. On the one hand, the flutter analysis can be performed according to the conventional linear analysis process in the frequency domain and on the other hand by means of coupled, dynamically fully nonlinear, time accurate simulations. Both approaches are followed in the present study. The results are compared to experimental data.

The conventional flutter analysis comprises the determination of the GAFs based on the structural eigenmodes. For each Mach number, GAF-matrices are computed at 9 equally spaced reduced frequencies ranging from $k_{red} = 0$ to $k_{red} = 2.35$, where k_{red} is calculated with respect to the semi aerodynamic mean chord $l_{ref} = 0.235\,m$. Each GAF-matrix has 5×5 complex entries and is computed with the small disturbance solver AER-SDNS that has already been applied to a low aspect ratio wing test case, see [31]. Since the eigenmodes are arbitrarily scalable and the small disturbance condition has to be met, the maximum deflection of each mode is restrained to approximately 3% of the wing root chord. The GAFs together with the modal mass and stiffness matrix form the input for the flutter solver. Because no information is available concerning the structural damping, it is neglected. As flutter solver, the g-method [32] is applied to determine the critical flutter velocity and flutter frequency for each Mach number listed in Tab. 4.

To assess the stability of the aeroelastic sytem based on nonlinear, transient, time accurate simulations, a computationally expensiv simulation has to be executed for every free stream condition of interest. Therefore an initial guess is made, regarding the critical dynamic pressure. At the beginning of each simulation, the wing tip is exposed to a vertical force and a twisting moment in order to impose an initial disturbance onto the aeroelastic system. Then, one simulation is conducted for undercritical free stream conditions and one for overcritical free stream conditions. Afterwards the damping coefficients are calculated from the obtained responses and are interpolated linearly. The root of the interpolated damping line provides the critical flutter velocity. Figure 4 shows exemplary results for a stable, an indifferent and an unstable response at $M_\infty = 0.678$. The physical time step size is chosen to be $\Delta t = 0.001\,s$. Comparing the dynamic pressure of the neutral response to the critical dynamic pressure determined by the interpolation, an insignificant deviation of $\Delta q_\infty = 0.4\,\%$ is observed. When

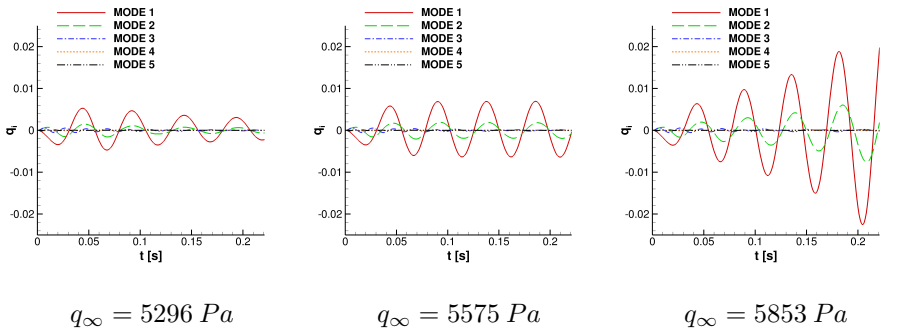

$q_\infty = 5296\ Pa$ $q_\infty = 5575\ Pa$ $q_\infty = 5853\ Pa$

Figure 4: Response of the generalized coordinates $\boldsymbol{q_i}$ of the AGARD 445.6 wing at $M_\infty = 0.678$, $\rho_\infty = 0.0995 kg/m^3$ and $\alpha = 0°$

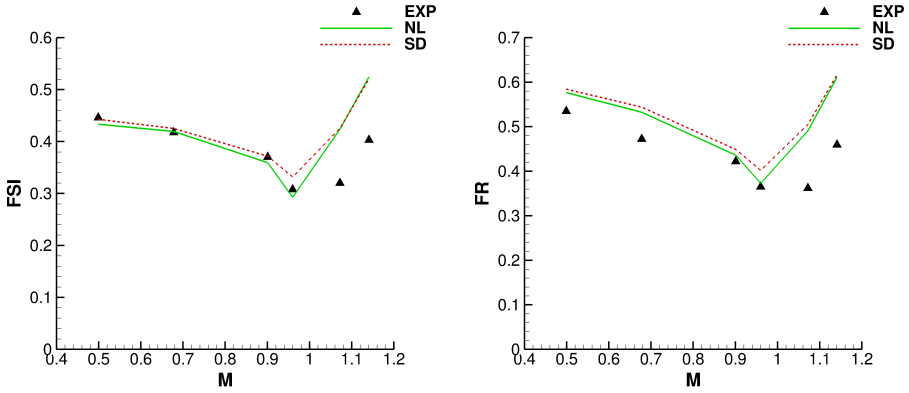

Figure 5: FSI and FR of the AGARD 445.6 wing at $\alpha = 0°$; EXP: Experimental data [13]; NL: Time domain simulation; SD: Frequency domain simulation

the aeroelastic system dynamics are dominated by considerable aerodynamic or structural nonlinearities, the transient, nonlinar method provides better results than the more efficient frequency domain approach.

The AGARD 445.6 test case is characterized by a coupling of the first bending and the first torsional mode. This flutter mechanism dominates the entire investigated Mach number range. Both, the flutter speed index (FSI) and the corresponding frequency ratio (FR) are plotted for the experiment (EXP), the nonlinear time domain simulation (NL) and the linearized frequency domain simulation (SD) in Fig. 5. The FSI and the FR are defined as

$$FSI = \frac{2V}{l_r \omega_\alpha \sqrt{\mu}}, \tag{39}$$

and

$$FR = \frac{\omega}{\omega_\alpha}, \tag{40}$$

where the flutter velocity V and the angular frequency ω are normalized by the angular frequency of the first torsional mode ω_α, the root chord length l_r and the mass ratio μ. Both plots show very similar characteristics. In the subsonic regime, the FSI as well as the FR decrease with increasing Mach number until they reach a minimum located at $M_\infty = 0.960$. This characteristic is known as "transonic dip". Especially in proximity of this region, CFD-methods offer much better predictions than potential flow methods. In the supersonic regime, FSI and FR increase monotonically. Both numerical methods provide very similar results, capturing transonic effects. The nonlinear method agrees slightly better with the experimental data due to nonlinear shock motion. At subsonic free stream velocities the predicted FSI agrees very well with the experimental data while the FR is overpredicted. In the supersonic Mach number range both numerical methods provide similar results but fail to reproduce the experimental data correctly. Other publications have demonstrated that the consideration of structural damping would yield better results for supersonic Mach numbers [33].

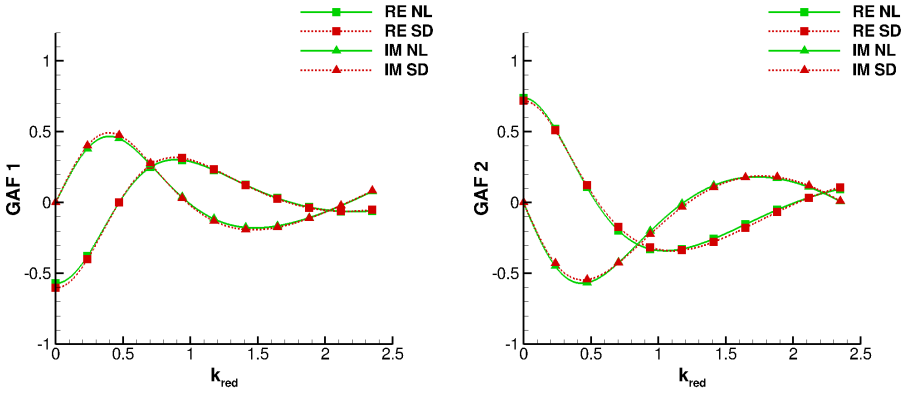

Figure 6: Gust-GAFs of the first and second eigenmode of the AGARD 445.6 wing at $M_\infty = 0.499$ and $\alpha = 0°$; RE: Real part; IM: Imaginary part; NL: Time domain simulation; SD: Frequency domain simulation

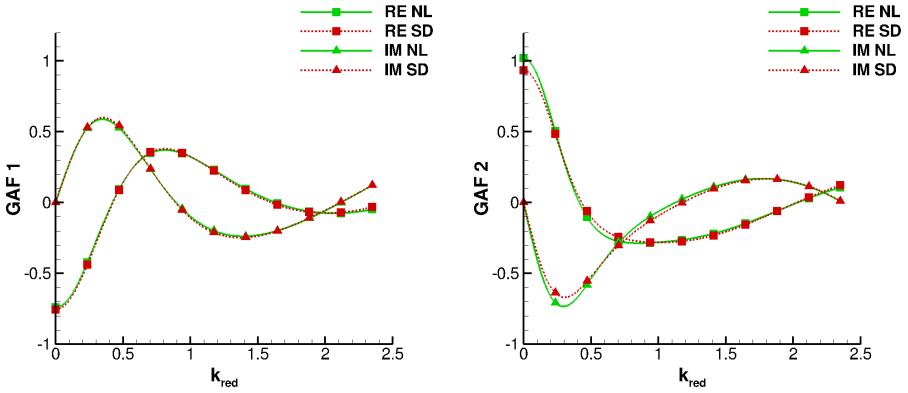

Figure 7: Gust-GAFs of the first and second eigenmode of the AGARD 445.6 wing at $M_\infty = 0.960$ and $\alpha = 0°$; RE: Real part; IM: Imaginary part; NL: Time domain simulation; SD: Frequency domain simulation

3.3 Discrete Gust Response in the Time and the Frequency Domain

In this section, the prediction qualities of the linear gust model implemented in the framework of the small disturbance solver AER-SDNS are demonstrated. Because experimentally determined gust responses are not readily available, the results provided by the linear gust model are compared to the results provided by the nonlinear gust model, serving as a baseline. Again the "weakened model 3" of the AGARD 445.6 wing is considered at the Mach numbers $M_\infty = 0.499$, $M_\infty = 0.960$ and $M_\infty = 1.141$.

The necessary input in order to generate a linear state space model comprises the gust induced GAFs, the modal structural matrices and the deformation induced GAFs. The gust induced GAF-vector is of dimension 5 corresponding to the number of considered structural eigenmodes. The GAFs are again computed at 9 discrete reduced frequencies ranging from $k_{red} = 0$ to $k_{red} = 2.35$. Additionally, the gust induced GAFs depend on the gust reference point located at the intersection point of the wing leading edge with the wing root. Fig. 6 to Fig. 8 depict the real (RE) and the imaginary (IM) part of the first bending mode (GAF 1) and the first torsional mode (GAF 2) computed by the nonlinear solver AER-NS (NL) and by the small disturbance solver AER-SDNS (SD). In case of the nonlinear solver, a time series of the GAFs is Fourier-analyzed and the resulting complex first order Fourier coefficients represent the sought-after GAF values. The GAF-functions presented in Fig. 6 to Fig. 8 are interpolated by the RFA-method according to Roger [27]. The oscillating shape of the plotted curves is evidence of the spiral character which is typically observed for gust loads plotted in the complex plane. From a qualitative point of view, the GAF-curves are independent of the Mach number. Quantitatively, differences can be observed. The GAFs are greater regarding their absolute values, especially in the transonic regime. The agreement between the numerical methods is very good. For all considered Mach numbers, the small disturbance solver is able to predict the gust induced GAFs for the AGARD 445.6 test case accurately.

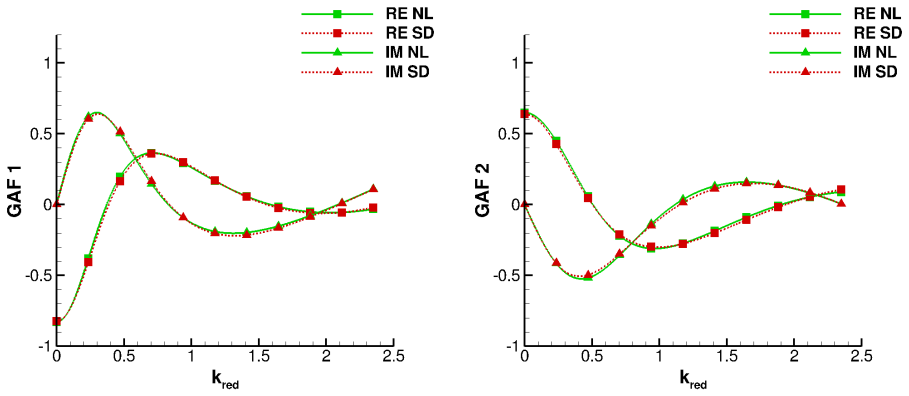

Figure 8: Gust-GAFs of the first and second eigenmode of the AGARD 445.6 wing at $M_\infty = 1.141$ and $\alpha = 0°$; RE: Real part; IM: Imaginary part; NL: Time domain simulation; SD: Frequency domain simulation

The properties of the four different vertical "1-cos"-gust functions that are investigated in the present study are listed in Tab. 5. The gust length and amplitude is chosen according to the guidelines [34], [35] and with respect to the structural eigenfrequencies. The free stream velocity is chosen to supply a damped and stable response. The gust length of $l_G = 5\,m$ and $l_G = 50\,m$ correspond to an excitation time of $t = 0.05\,s$ and $t = 0.5\,s$, respectively. The induced velocity amplitudes $v_G = 2\,m/s$ and $v_G = 10\,m/s$ correspond to an angle of attack of $\alpha = 1.15°$ and $\alpha = 5.71°$, respectively. The physical time step size employed for the nonlinear coupled method as well as for the solution of the linear state space model is $\Delta t = 0.001s$.

The discrete gust responses of the generalized coordinates corresponding to the first bending mode (MODE 1) and the first torsional mode (MODE 2) are plotted in Fig. 9 to Fig. 11 for the Mach numbers $M_\infty = 0.499$, $M_\infty = 0.960$ and $M_\infty = 1.141$. The total simulation time corresponds to a period of $t = 1\,s$. Again, the nonlinear time domain approach (NL) is compared to the small disturbance frequency approach (SD), which results in a linear state space model. Common to all plotted results is the observation that both eigenmodes are excited, but the bending mode deflection is much greater compared to the wing twist. After the gust has passed the wing, it performs a damped oscillation until it converges to the equilibrium position. Furthermore, as expected for a linear method, the response amplitude scales with the gust amplitude. Surprisingly, the wing is deflected stronger in case of the short gust $l_G = 5\,m$ than for $l_G = 50\,m$, despite being exposed to the gust for a shorter period of time. This is due to the fact that the short gust excitation frequency lies much closer to the first eigenfrequency of the wing. In addition, the damping is stronger in the case of the long gust $l_G = 50\,m$. Comparing the linear with the nonlinear method, it can be generally observed, that the deflection amplitude is slightly smaller and the response is delayed up to $\Delta t = 0.01s$ for the latter result. This behavior is caused by dissipative numerical effects.

Figure 9 depicts the results for the subsonic Mach number $M_\infty = 0.499$. In case of the small gust amplitude, a maximum wing deflection of 2.3 % l_r and in case of the strong gust amplitude, a maximum wing deflection of 11.5 % l_r is observed. Beyond $t = 0.8\,s$, the oscillations have mostly subsided. The comparison of the linear and nonlinear methods shows very good agreement.

Figure 10 depicts the resultsfor the transonic Mach number $M_\infty = 0.960$. Especially in the case of the long gust length in combination with the large amplitude, major differences can be observed. For the nonlinear simulation, the maximum deflection of the first eigenmode is significantly greater than for the linear method, as nonlinear flow phenomena are accounted for. In addition, oscillations of the first eigenmode are excited much stronger than in the linear case. This can be observed best for the long gust with the small amplitude. The predicted damping is much smaller than in the subsonic case, although the free stream velocity is significantly below the critical flutter velocity. In

Table 5: Properties of the investigated "1-cos"-gust cases

Free stream velocity U_∞ in m/s	Gust length l_G in m	Gust amplitude v_G in m/s
100	50	2
100	50	10
100	5	2
100	5	10

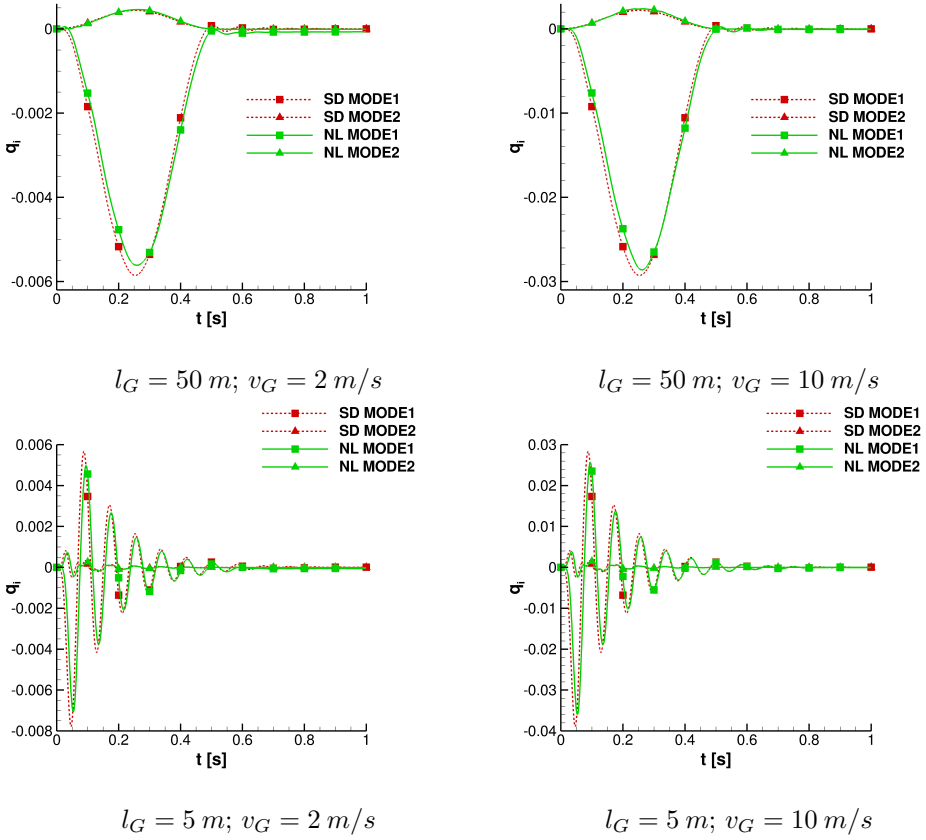

$l_G = 50\,m;\ v_G = 2\,m/s$ $l_G = 50\,m;\ v_G = 10\,m/s$

$l_G = 5\,m;\ v_G = 2\,m/s$ $l_G = 5\,m;\ v_G = 10\,m/s$

Figure 9: Gust response of the AGARD 445.6 wing for a "1-cos"-excitation at $M_\infty = 0.499$, $U_\infty = 100\ m/s$ and $\alpha = 0°$; NL: Time domain simulation; SD: Frequency domain simulation

the nonlinear case, the wing oscillations do not completely decay to zero wing deflection. This is caused by small asymmetries in the numerical model that are revealed due to very small wing deflection amplitudes of $0.5\,\%\,l_r$. In contrast to the subsonic case, the oscillation frequency predicted by the nonlinear method is smaller than the oscillation frequency predicted by the linear method, observed especially for the short gust excitation.

Figure 11 depicts the results belonging to the supersonic Mach number $M_\infty = 1.141$. The results are very similar to the responses at transonic flow conditions. The overall agreement is very good as long as the deflection amplitudes are not too small.

4 Conclusions

Two different numerical approaches have been implemented in an in-house aeroelastic solver for stability and response analysis. The main focus of the present study is on load prediction due to discrete gust impact. One method is based on a linear small disturbance frequency domain formulation. The other method is based on a nonlinear coupling procedure in time domain. The aeroelastic prediction quality was first validated with experimental data by means of

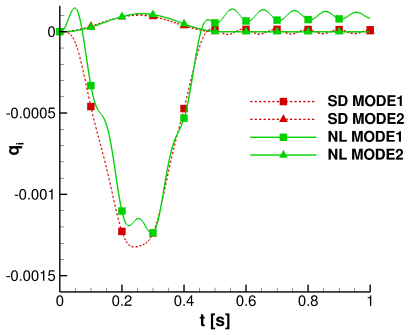

$l_G = 50\,m;\ v_G = 2\,m/s$

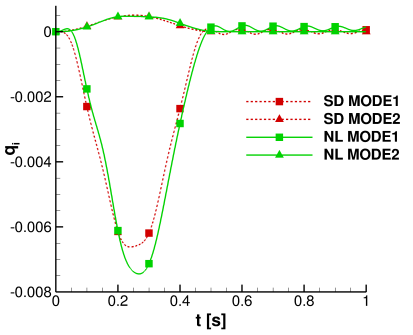

$l_G = 50\,m;\ v_G = 10\,m/s$

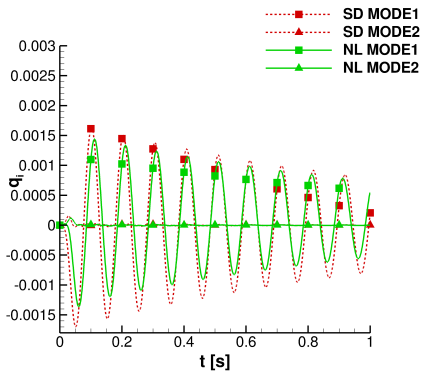

$l_G = 5\,m;\ v_G = 2\,m/s$

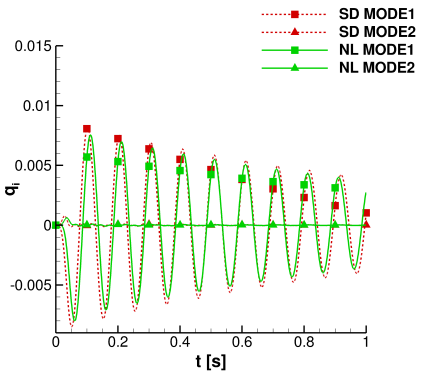

$l_G = 5\,m;\ v_G = 10\,m/s$

Figure 10: Gust response of the AGARD 445.6 wing for a "1-cos"-excitation at $M_\infty = 0.960$, $U_\infty = 100\,m/s$ and $\alpha = 0°$; NL: Time domain simulation; SD: Frequency domain simulation

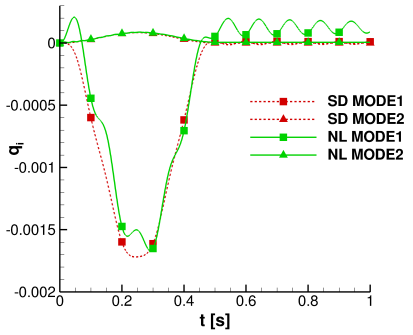

$l_G = 50\,m;\ v_G = 2\,m/s$

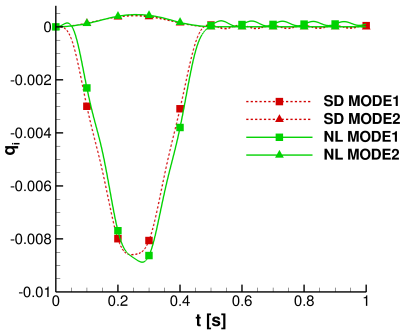

$l_G = 50\,m;\ v_G = 10\,m/s$

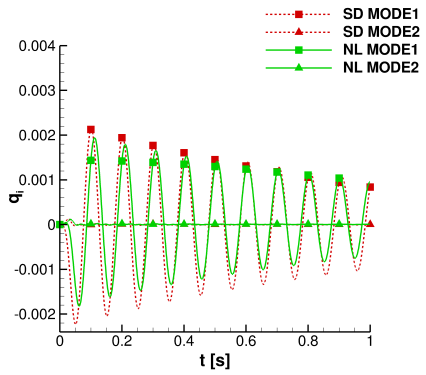

$l_G = 5\,m;\ v_G = 2\,m/s$

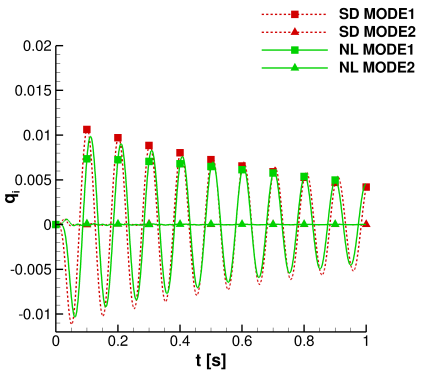

$l_G = 5\,m;\ v_G = 10\,m/s$

Figure 11: Gust response of the AGARD 445.6 wing for a "1-cos"-excitation at $M_\infty = 1.141$, $U_\infty = 100\,m/s$ and $\alpha = 0°$; NL: Time domain simulation; SD: Frequency domain simulation

a stability analysis. The test case is the low aspect ratio swept AGARD 445.6 wing with Mach numbers ranging from the subsonic to the supersonic. Both methods are able to predict the "transonic dip" and show nearly similar results. The results of the nonlinear method agree better with the experimental data at transonic Mach numbers.

The small disturbance solver has been extended by a gust model based on an artificial disturbance velcocity approach, which is capable of predicting complex GAFs. The GAFs are interpolated and substituted into a linear state space model. Aeroelastic time responses were computed using the linear approach and compared to nonlinear, coupled time domain results. The overall agreement between both methods is very good. Small deviations are observed due to transonic effects, especially nonlinearly moving shocks, that cannot be predicted accurately by the linear method. Additionally, differences in the oscillation frequencies of the single modal coordinates are observed and the nonlinear scheme is slightly more dissipative. The linear methodology is observed to be very robust and efficient. It can be used within the established aeroelastic tool chains without any modifications.

References

[1] Henshaw, M. J. de C., Badcock, K. J., Vio, G. A., Allen, C. B., Chamberlain, J., Kaynes, I., Dimitriadis, G., Cooper, J. E., Woodgate, M. A., Rampurawala, A. M., Jones, D., Fenwick, C., Gaitonde, A. L., Taylor, N. V., Amor, D. S., Eccles, T. A., Denley, C. J., *Non-linear aeroelastic prediction for aircraft applications*, Journal of Progress in Aerospace Sciences 43, 2007.

[2] Dowell, E., Edwards, J., Strganac, T., *Nonlinear Aeroelasticity*, Journal of Aircraft, Vol. 40, No. 5, 2003.

[3] Schuster, D. M., Liu, D. D., Huttsell, L. J., *Computational Aeroelasticity: Success, Progress, Challenge*, Journal of Aircraft, Vol. 40, No. 5, 2003.

[4] Küssner, H. G., *General Airfoil Theory*, Luftfahrtforschung, Vol. 17, 1940.

[5] Sears, W. R., *Some Aspects of Non-Stationary Airfoil Theory and Its Practical Applications*, Journal of the Aeronautical Sciences, Vol. 8, No. 3, 1941.

[6] Lucia, D. J., Beran, P. S., Silva, W. A., *Reduced-order modeling: new approaches for computational physics*, Progress in Aerospace Sciences 40, 2004.

[7] Dowell, E. H., Hall, K. C., *Modeling of fluid-structure interaction*, Annual Review of Fluid Mechanics, 33, 2001.

[8] Pechloff, A., Laschka, B., *Small Disturbance Navier-Stokes Method: Efficient Tool for Predicting Unsteady Air Loads*, Journal of Aircraft, Vol. 43, No. 1, 2006.

[9] Iatrou, M., *Ein Navier-Stokes-Verfahren kleiner Störungen für instationäre Vorgänge - Anwendung auf Transportflugzeuge*, Dissertation, Lehrstuhl für Aerodynamik, TU München, 2010.

[10] Zhang, Z., Yang, S., Chen, P. C., *Linearized Euler Solver for Rapid Frequency-Domain Aeroelastic Analysis*, Journal of Aircraft, Vol. 49, No. 3, 2012.

[11] Heinrich, R., *Comparison of Different Approaches for Gust Modeling in the CFD Code TAU*, IFASD-Paper, Bristol, 2013.

[12] Jirasek, A., *CFD-Analysis of Gust Using Two Different Gust Models*, RTO AVT-189 Paper, Portsdown West, 2011.

[13] Yates, E. C., Jr., *AGARD Standard Aeroelastic Configurations for Dynamic Response. Candidate Configuration I.-Wing 445.6*, AGARD, Report No. 765, 1987.

[14] Roe, P. L., *Approximate Riemann Solvers, Parameter Vectors and Difference Schemes*, Journal of Computational Physics, Vol. 43, No. 2, 1981.

[15] Chakravarthy, S. R., *High Resolution Upwind Formulations for the Navier-Stokes-Equations*, Von Kármán Inst. Lecture Series on Computational Fluid Dynamics, VK-I 1988-05, Brüssel, 1988.

[16] Kreiselmaier, E., Laschka, B., *Small Disturbance Euler Equations: Efficient and Accurate Tool for Unsteady Load Prediction*, Journal of Aircraft, Vol. 37, No. 5, 2000.

[17] Blazek, J., *Computational Fluid Dynamics: Principles and Applications*, ACADEMIC PR INC, 2005.

[18] Blazek, J., *A Multigrid LU-SSOR Scheme for the Solution of Hypersonic Flow Problems*, AIAA-Paper 94-0062, 1994.

[19] Hirsch, C., *Numerical Computation of Internal and External Flows, Vol. 2, Computational Methods for Inviscid and Viscous Flows*, John Wiley and Sons, New York, 1991.

[20] Spalart, P. R., Allmaras, S. R., *A One Equation Turbulence Model for Aerodynamic Flows*, AIAA-Paper 92-0439, 1992.

[21] Iatrou, M., Weishäupl, C., and Laschka, B., *Entwicklung eines Instationären Navier-Stokes-Verfahrens bei Kleinen Störungen für Aeroelastische Problemstellungen*, Institute for Fluid Mechanics, Technische Universität München, Report TUM-FLM-2002/9, Garching, Germany, 2002.

[22] Alonso, J. J., Jameson, A., *Fully Implicit Time-Marching Aeroelastic Solutions*, AIAA-Paper 94-0056, 1994.

[23] Zaide, A., Raveh D., *Numerical Simulation and Reduced Order Modeling of Airfoil Gust Response*, AIAA-Paper 2005-5128, Toronto, 2005.

[24] Braun, C., *Ein modulares Verfahren für die numerische aeroelastische Analyse von Luftfahrzeugen*, Dissertation, Fakultät für Matehmatik, Informatik und Naturwissenschaften, RWTH Aachen, 2007.

[25] Duchon, J. P., *Splines Minimizing Rotation-Invariant Semi-Norms in Sobolev Spaces*, Constructive Theory of Functions of Several Variables, Springer-Verlag, Berlin, 1977.

[26] Tsai, H. M., Wong, A. S. F., Cai, J., Zhu, Y., Liu, F., *Unsteady Flow Calculations with a Parallel Multiblock Moving Mesh Algorithm*, AIAA Journal, Vol. 39, No. 6, 2001.

[27] Roger, K. L., *Airplane Math Modeling Methods and Active Aeroelastic Control Design*, AGARD-CP-228, 1977.

[28] Smith, T. A., Hakanson, J. W., Nair, S. S., *State-Space Model Generation for Flexible Aircraft*, Journal of Aircraft, Vol. 41, No. 6, 2004.

[29] Kolonay, R. M., *Unsteady Aeroelastic Optimization in the Transonic Regime*, Ph.D. Thesis, Dept. of Aeronautics and Astronautics, Purdue Univ., Lafayette, 1996.

[30] Fleischer, D., *Verfahren reduzierter Ordnung zur Ermittlung instationärer Luftkräfte*, Dissertation, Lehrstuhl für Aerodynamik, TU München, 2014.

[31] Pechloff, A., Laschka, B., *Small Disturbance Navier-Stokes Computations for Low-Aspect-Ratio Wing Pitching Oscillations*, Journal of Aircraft, Vol. 47, No. 3, 2010.

[32] Chen, P. C., *A Damping Perturbation Method for Flutter Solution: The g-Method*, AIAA Journal, Vol. 38, No. 5, 2000.

[33] Lee-Rausch, E. M., Batina, J. T., *Wing Flutter Computations Using an Aerodynamic Model Based on the Navier-Stokes Equations*, Journal of Aircraft, Vol. 33, No. 6, 1996.

[34] EASA, *Certification Specifications for Large Aeroplanes CS-25*, European Aviation Safety Agency, 2010.

[35] *Military Specification - Flying Qualities of Piloted Airplanes*, Technical Report MIL-F-8785C, 1980.